Supplementary Material: Multipartite entanglement in a microwave frequency comb

Shan W. Jolin,[1, *] Gustav Andersson,[2, 3] J. C. Rivera Hernández,[1] Ingrid Strandberg,[3] Fernando Quijandría,[3, †] José Aumentado,[4] Riccardo Borgani,[1, 5] Mats O. Tholén,[1, 5] and David B. Haviland[1]

[1]*Department of Applied Physics, KTH Royal Institute of Technology, SE-106 91 Stockholm, Sweden*
[2]*Pritzker School of Molecular Engineering, University of Chicago, Chicago, Illinois 60637, USA*
[3]*Department of Microtechnology and Nanoscience MC2,*
Chalmers University of Technology, SE-412 96 Göteborg, Sweden
[4]*National Institute of Standards and Technology, 325 Broadway, Boulder, CO 80305, USA*
[5]*Intermodulation Products AB, SE-823 93 Segersta, Sweden*

I. MEASUREMENT SETUP

The Josephson parametric amplifier (JPA) is cooled to 10 mK with a dilution refrigerator and operated in reflection, which means that the input and output share the same port. The two opposite travelling waves are separated by a circulator (see Fig. **??**a) permitting us to further amplify only the outgoing signal. A pair of isolators prevents noise from the following amplifier from reaching the JPA signal port.

An RF pump applied at a second port modulates the flux in the JPA SQUID. We also apply a DC current through the pump port to tune the JPA resonance down to 4.2 GHz. A diplexer at the 10 mK-stage of the dilution refrigerator combines the DC current and RF pumps. See Fig. S1 for schematic description of the entire measurement setup. We pump at twice the JPA resonance frequency using external signal generators locked to the measurement sampling clock.

Measurement of the noise covariance is performed with Vivace from Intermodulation Products [1] running a continuous wave firmware which implements a multifrequency lockin amplifier. The lockin is designed to work with orthogonal frequencies on the time-window used for demodulation. A process refered to as tuning fixes the drive and measurement frequencies such that they are integer multiples of the measurement bandwidth (inverse of the time window) while being commensurate with the sampling frequency [2, 3].

Based on the latest Radio Frequency System-on-a-Chip (RFSoC) technology, Vivace uses fast Digital-Analog Converters (DAC) at 5 GSamples/s, resulting in a Nyquist frequency of 2.5 GHz. We operate the DAC in the second Nyquist zone to directly access the microwave noise. Bandpass filters select the noise in the second Nyquist zone, measured at its alias frequency in the 1st zone, while rejecting noise at that frequency in the 1st zone. This digital method of down conversion eliminates analog mixers, thus removing another source of error from improperly calibrated mixers [4]. We use a bandpass filter at the warm amplifier stage to prevent aliasing when sampling the noise. However the filter (VBFZ-5500-S+) has a specified range of 4.9–6.2 GHz, meaning that measurements at 4.3 GHz suffer from additional loss.

II. CALIBRATION

To reconstruct the quantum state before amplification, we need an accurate estimate of the gain and added noise of the entire amplification chain. If we consider the amplification chain as a noisy bosonic Gaussian channel [**?**] where each mode, labelled by index n, is subject to a frequency-dependent gain G_n and an average number of added noise photons $\bar{n}_n$. Amplification transforms the multimodal quantum covariance matrix V' into the measured covariance matrix $\tilde{V}$ according to

$$\tilde{V} = TV'T^{\top} + N, \tag{S1}$$

where $T = \bigoplus_n \sqrt{G_n} I_n$ and $N = \bigoplus_n (G_n - 1)(2\bar{n}_n + 1)I$. Here $\bigoplus$ is the direct sum and I the identity matrix. By inverting T, the quantum covariance matrix V' is reconstructed according to

$$V' = T^{-1}\left(\tilde{V} - N\right)(T^{\top})^{-1}, \tag{S2}$$

using calibrated values for G_n and $\bar{n}_n$. All our expressions assume covariance matrices are normalized such that the vacuum state corresponds to the identity matrix.

We estimate parameters G_n and $\bar{n}_n$ by measuring the noise emitted from a matched resistor $R = 50\,\Omega$ as a function of the temperature T, a method known as Planck spectroscopy [5, 6]. This black-body noise is reflected off of the quiescent JPA, operated with no flux pump or flux bias. There are two noise sources: the -20 dB attenuator on the input signal line to the JPA and the matched load of the isolators, both at the 10 mK-stage. Their temperature is controlled by slowly heating up the entire 10 mK-stage, allowing the temperature to stabilize for 20 min before measuring.

The power spectral density of the noise is given by [7]

$$P = \frac{\hbar\omega}{2}\coth\frac{\hbar\omega}{2kT}. \tag{S3}$$

---

[*] shan@meetiqm.com; Present address: IQM Finland Oy, Espoo 02150, Finland

[†] Present address: Quantum Machines Unit, Okinawa Institute of Science and Technology Graduate University, Onna-son, Okinawa 904-0495, Japan

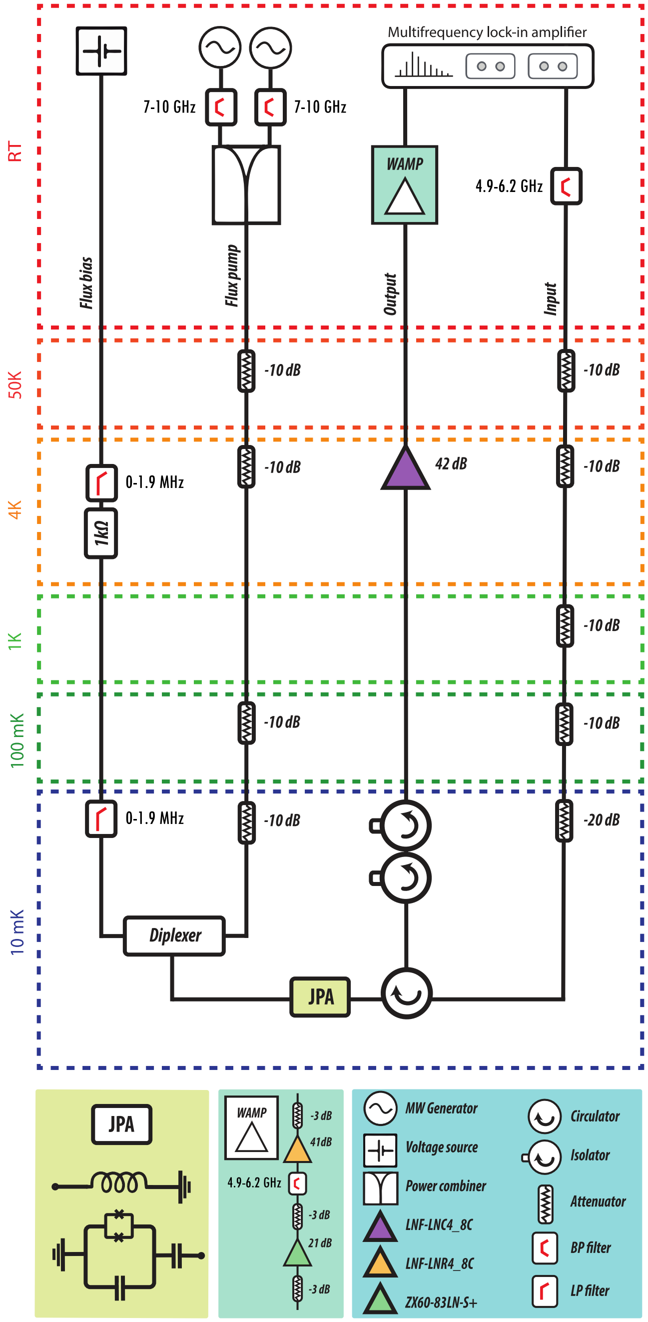

FIG. S1. Schematic of complete measurement setup including cryogenic electronics. Note that despite the JPA signal input is connected to our multi-frequency lockin, it was not used in the measurements presented in the main text. A signal was provided only for characterization purposes. Here we use a bandpass filter in the warm amplifier (WAMP) stage to 4.9–6.2 GHz range with the purpose to reduce aliasing.

An amplifier scales this noise power by the gain G and adds an average number of noise photons $\bar{n}$,

$$P = G\hbar\omega\left[\frac{1}{2}\coth\frac{\hbar\omega}{2kT}+\frac{1}{2}(1+2\bar{n})\right]. \qquad \text{(S4)}$$

In terms of the voltage variance over a measurement bandwidth Δ_f this expression reads

$$\langle V^2\rangle = 4\Delta_f G\hbar\omega R\left[\frac{1}{2}\coth\frac{\hbar\omega}{2kT}+\frac{1}{2}(1+2\bar{n})\right]. \qquad \text{(S5)}$$

Note that even if the added noise $\bar{n}=0$, there is always a half-photon of added noise power, which reflects the nature of phase insensitive amplification [8]. Figure S2a depicts the fit of Eq. (S4) to the noise power, there expressed instead in units of photon number at the amplifier input (hence this quantity is divided by the amplifier gain) called the input referred photon number.

The noise power for the calibration is obtained at all frequencies simultaneously (in the same time window) with the multifrequency lockin. The data (Fig. S2a) clearly shows the flattening at lower temperatures, revealing the measurement of quantum fluctuations. The extracted gain G and $\bar{n}$ as a function of frequency is shown in Fig. S2b and Fig. S2c respectively. Heating the 10 mK-stage in this manner places the reference plane for the calibration (as seen by the amplifier) close to the first isolator and after the JPA. A better calibration procedure that takes in to account the small insertion losses of the isolator and circulator, is expected to improve the purity of our reconstructed data.

III. JOSEPHSON PARAMETRIC AMPLIFIER

The JPA is fabricated in the NIST Boulder cleanroom using an optical lithography process for multi-layer superconducting circuits with niobium trilayer junctions. The layer stack details are given in the appendix of Ref. [9]. The circuit, shown in Fig. S3, has a parallel LC resonance, where $C \approx 12\,pF$ is realized by an overlap capacitor with low-loss amorphous silicon as the dielectric ($\epsilon \approx 9$, $\tan\delta \sim$1.5–5$\times 10^{-5}$). L is the Josephson inductance of a gradiometric dc-SQUID, with junction critical currents, $I_0 \simeq 5\,\mu$A, giving a total SQUID critical current, $I_{\mathrm{SQ}} \simeq 10\,\mu$A. The SQUID's Josephson inductance is modulated with external magnetic flux from a flux line. The flux port is driven by a diplexer (see fig. S1) for both DC bias and AC pumping. The circuit was designed for a maximum resonant frequency of approximately 8 GHz. At zero flux bias the resonance is found at 7.8 GHz. The resonator is coupled to the signal port through a capacitance $C_c \approx 0.5\,$pF which fixes the loaded bandwidth of the JPA.

For entanglement measurements we bias the JPA resonance with DC flux to achieve $\omega_0/2\pi \approx 4.3\,$GHz ($\Phi_{\mathrm{dc}} \simeq \pm 0.4\Phi_0$), where we measure a loaded bandwidth of $\kappa \approx 124\,$MHz. At this flux bias, where the slope of the resonance frequency versus flux is roughly linear, we modulate (pump) the flux at $\Omega_{1,2} \sim 2\omega_0$ to generate 3-wave mixing (in contrast to 4-wave mixing or 'doubly-degenerate' pumping where $\Omega_{1,2} \sim \omega_0$). Three-wave mixing has the advantage that pump-to-signal port leakage, which may interfere with measurements of multi-mode entanglement, is far from the mode frequencies of interest.

For all entanglement tests we operate the JPA at relatively low pump power. For the monochromatic case the applied output pump power at the signal generator output is $-3\,$dBm. With a bichromatic pump however, we operate the JPA with each pump at $-7\,$dBm. Fig. S4 shows the power dependence of the noise power spectral density (PSD) emitted by the JPA subjected to a bichromatic pump. At $-3\,$dBm a Lorentzian-like shape appears, indicating gain in the JPA. At $-7\,$dBm we see that the PSD lifts slightly above the pump-off reference (solid line). We found that $-3\,$dBm added too much noise to the data for investigation of multi-modal entanglement, but $-7\,$dBm was a good compromise between strong correlations and low added noise. The shaded region indicates the frequency range where the entangled modes from the main text can be found.

IV. COVARIANCE MATRIX RECONSTRUCTION

A. Error propagation

The experimental errors in the covariance matrix V' should take into account uncertainties in both the measurement and the calibration. We estimate measurement errors by applying a bootstrap method (see [10] for a pedagogical discussion) to each element in the covariance matrix. The two sources of error are appropriately combined through error propagation based on Eq. (S2) in the main text (assuming $G \gg 1$), to obtain an estimate of the uncertainty of each element in V', expressed as an error matrix σ_{nm}.

$$\sigma_{nm}^2 = \begin{cases} \left(\frac{\sigma_n^G \tilde{V}_{nn}}{G_n^2}\right)^2 + (2\sigma_n^{\bar{n}})^2 + 4\frac{\tilde{V}_{nn}\sigma_i^{G\bar{n}}}{G_i^2} + \left(\frac{\sigma_{nm}^{\tilde{V}}}{G_n}\right)^2 \\ \qquad \text{if } n = m, \\ \left(\frac{\sigma_n^G \tilde{V}_{nm}}{2\sqrt{G_n^3 G_m}}\right)^2 + \left(\frac{\sigma_m^G \tilde{V}_{mn}}{2\sqrt{G_m^3 G_n}}\right)^2 + \left(\frac{\sigma_{nm}^{\tilde{V}}}{\sqrt{G_n G_m}}\right)^2 \\ \qquad \text{if } n \neq m, \end{cases} \tag{S6}$$

where σ_n^G and $\sigma_n^{\bar{n}}$ are uncertainties in the parameters G and $\bar{n}$. As we cannot assume these are completely independent, their covariance $\sigma_n^{G\bar{n}}$ has to be accounted for. The measurement errors in $\tilde{V}_{nm}$ are denoted $\sigma_{nm}^{\tilde{V}}$.

For the SvL criteria Eq. (**??**), the uncertainty in the quantity $\mathcal{E}$ is estimated using error propagation, for which the result is

$$\delta\mathcal{E} = \sqrt{\sum_{\alpha\beta}\left((\sigma^{II})^2_{\alpha\beta} h_\alpha^2 h_\beta^2 + (\sigma^{QQ})^2_{\alpha\beta} g_\alpha^2 g_\beta^2\right)}. \tag{S7}$$

The uncertainties in the covariance matrix are denoted by σ^{II} and σ^{QQ} (corresponds to the uncertainties in elements of V^{II} and V^{QQ} respectively, see the main text).

B. Additional details on data analysis

The optimization of Eq. (**??**) is performed by convex optimization [11, 12]. As mentioned in the main text, for each of the three subsets of independent modes, K^{-1}, K^0, K^1, we analyze six covariance matrices from which

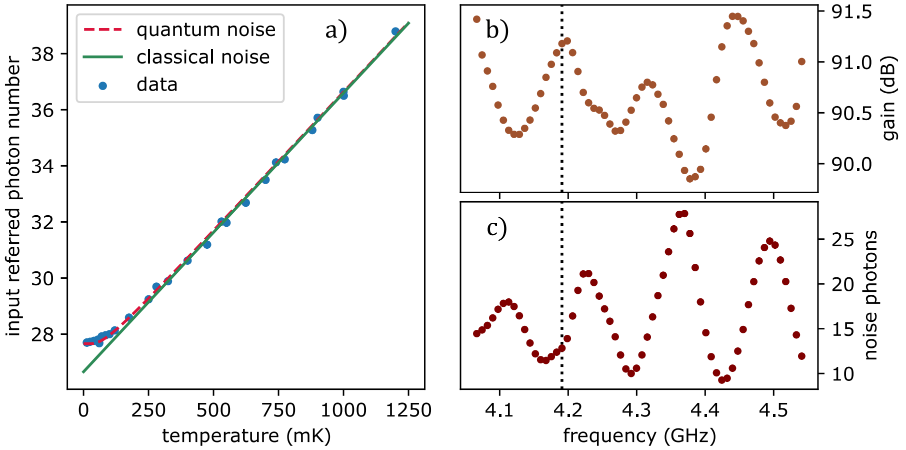

FIG. S2. **a**: Number of photons referred to the amplifier input. The fit provides with the values G (gain) and $\bar{n}$ (added noise) at the frequency specified by the dashed vertical line in figures b and c (at 4.19 GHz). The deviation from the green line is due to vacuum fluctuations. **b** and **c**: The gain and added noise is plotted as a function of frequency. In all figures, the errorbars indicating one standard deviation are smaller than the marker size.

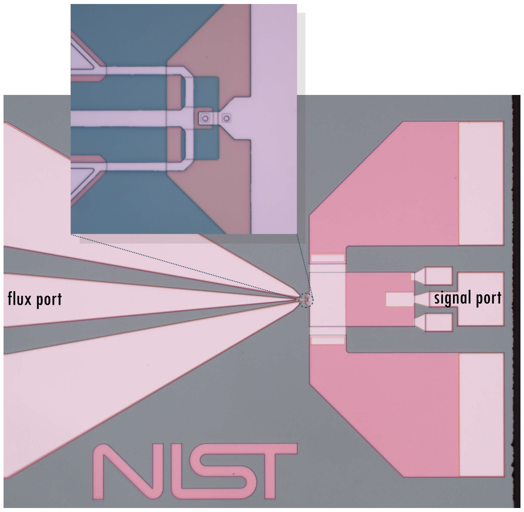

FIG. S3. An optical image of the JPA device with an inset zoomed in on the gradiometric dc-SQUID. Flux and signal parts are labelled. The width of the chip is about 5 mm.

a maximum value of 1.15σ, 0.95σ and 0.92σ standard deviations is obtained for each subset respectively. Each of the six matrices in each subset is tested for entanglement using (**??**) from the main text. Optimization is in this case carried out using differential evolution [13]. The results of these individual tests are shown in Fig. S5. Fig. **??** in the main text presents the weighted mean for each subset, which is calculated according to

$$\mathcal{E}_w = \frac{\sum_{k=1}^{6} w_k \mathcal{E}_k}{\sum_{k=1}^{6} w_k}, \quad \delta\mathcal{E}_w = \frac{1}{\sqrt{\sum_{k=1}^{6} w_k}}, \quad w_k = \frac{1}{\delta\mathcal{E}_k^2}. \tag{S8}$$

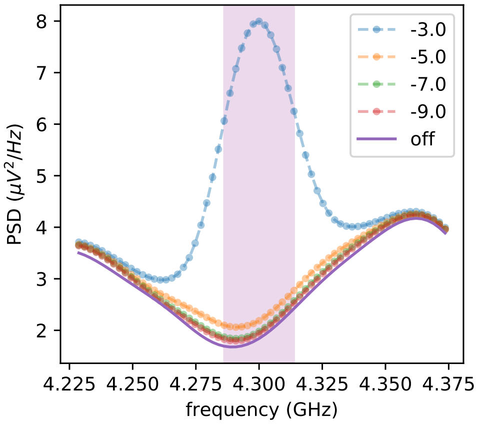

FIG. S4. The noise PSD from a bichromatically pumped JPA. The different colored lines indicate the pump power of each pump in dBm (both pumps are equal in power). For the entanglement tests, the JPA was operated at −7 dBm. The shaded region indicates the frequency range where the modes for our entanglement test reside.

V. COVARIANCE MATRIX OF OUTPUT NOISE

A. JPA Hamiltonian

The Hamiltonian for a resonator terminated in a Josephson junction is

$$H = \hbar\omega_r\, a^\dagger a - E_J \cos\left(\frac{\Phi}{\varphi_0}\right), \tag{S9}$$

where Φ is the total flux across the junction and $\varphi_0 = \hbar/2e$ is the reduced magnetic flux quantum. We expand

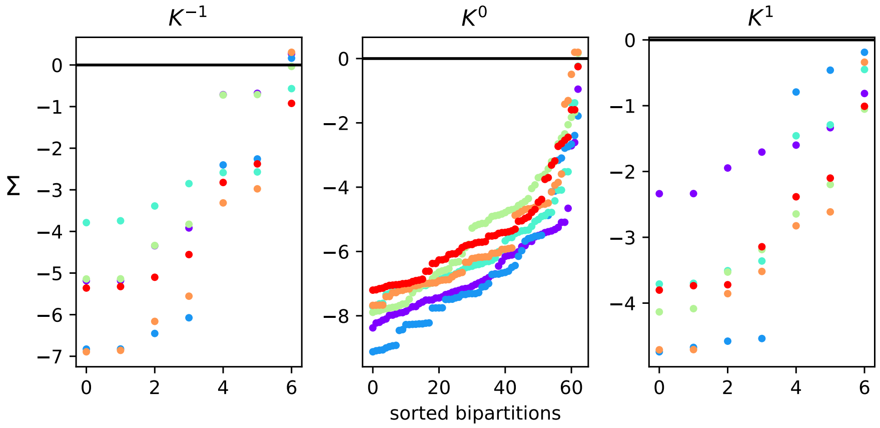

FIG. S5. We plot the SvL bipartition test result for the six covariance matrices in three mode subsets. Points with the same color stem from the same matrix. The weighted mean of points belonging to the same bipartition are the Σ_w points in the main text Fig. **??**.

the cosine up to second-order in Φ/φ_0

$$\cos\left(\frac{\Phi}{\varphi_0}\right) = 1 - \frac{1}{2!}\left(\frac{\Phi}{\varphi_0}\right)^2 + \mathcal{O}\left[\left(\frac{\Phi}{\varphi_0}\right)^3\right]. \tag{S10}$$

Discarding the constant term, we have

$$H = \hbar\omega_r\, a^\dagger a + \frac{E_J}{2!}\left(\frac{\Phi}{\varphi_0}\right)^2. \tag{S11}$$

Now, the flux field Φ is given by

$$\Phi = \phi_{\mathrm{ZPF}}(a^\dagger + a), \tag{S12}$$

where ϕ_{ZPF} correspond to the zero-point fluctuations (ZPF) in the flux. Then, we finally get for the Hamiltonian

$$H = \hbar\omega_r\, a^\dagger a + \frac{E_J}{2!}\phi_0^2(a^\dagger + a)^2, \tag{S13}$$

where we have introduced the reduced ZPF $\phi_0 \equiv \phi_{\mathrm{ZPF}}/\varphi_0$. This can be further simplified to

$$H = \hbar\widetilde{\omega}_r\, a^\dagger a + \frac{E_J}{2!}\phi_0^2(a^{\dagger 2} + a^2) \tag{S14}$$

by introducing the renormalized resonator frequency $\widetilde{\omega}_r = \omega_r + E_J\phi_0^2/\hbar$.

Replacing the Josephson junction by a DC SQUID, we gain tunability of the Josephson energy: $E_J \to E_J(\phi_{\mathrm{ext}}) = E_{J,0}\cos(\phi_{\mathrm{ext}})$. Consider the following time-dependent external magnetic flux

$$\phi_{\mathrm{ext}}(t) = \phi_{\mathrm{dc}} + \phi_{\mathrm{ac}}(t), \tag{S15}$$

where ϕ_{dc} is a time-independent bias and $\phi_{\mathrm{ac}}(t)$ is a small amplitude modulation supplied by a flux pump. The amplitude is small in the sense that $|\phi_{\mathrm{ac}}(t)/\phi_{\mathrm{dc}}| \ll 1$. In this regime we have different order approximations of the Josephson energy in the modulation amplitude. To first-order

$$\begin{aligned}\cos\phi_{\mathrm{ext}}(t) &= \cos\left(\phi_{\mathrm{dc}} + \phi_{\mathrm{ac}}(t)\right)\\ &= \cos\phi_{\mathrm{dc}} - \phi_{\mathrm{ac}}(t)\sin\phi_{\mathrm{dc}},\end{aligned} \tag{S16}$$

and second-order

$$\begin{aligned}\cos\phi_{\mathrm{ext}}(t) &= \cos\left(\phi_{\mathrm{dc}} + \phi_{\mathrm{ac}}(t)\right)\\ &= \cos\phi_{\mathrm{dc}}\cos\phi_{\mathrm{ac}}(t) - \sin\phi_{\mathrm{dc}}\sin\phi_{\mathrm{ac}}(t)\\ &= \cos\phi_{\mathrm{dc}}\left(1 - \frac{1}{2!}\phi_{\mathrm{ac}}(t)^2\right) - \phi_{\mathrm{ac}}(t)\sin\phi_{\mathrm{dc}}\\ &= \cos\phi_{\mathrm{dc}} - \left(\phi_{\mathrm{ac}}(t)\sin\phi_{\mathrm{dc}} + \frac{1}{2!}\phi_{\mathrm{ac}}(t)^2\cos\phi_{\mathrm{dc}}\right).\end{aligned} \tag{S17}$$

We find it sufficient to consider only up to first-order to qualitatively reproduce the features in our data. Notice that if we had not applied any static flux bias, i.e. $\phi_{\mathrm{dc}} = 0$, then the first-order expression Eq. (S16) would reduce to zero and the second-order expression Eq. (S17) would be necessary.

In this work we consider a modulation of the form

$$\phi_{\mathrm{ac}}(t) = \sum_{n=1}^{n_s} i\lambda_n \exp\left[-i(2\widetilde{\omega}_r + \delta_n)t\right] + \text{h.c.}, \tag{S18}$$

that is, a sum of n_s sinusoidal waves at near twice the resonator frequency. For a bichromatic pump, $n_s = 2$. Here λ_n denote the complex amplitudes and $|\delta_n| \ll \widetilde{\omega}_r$ the small detunings from $2\widetilde{\omega}_r$.

In the first-order approximation Eq. (S16), the Hamiltonian for the resonator and SQUID becomes

$$\begin{aligned}H \approx{}& \hbar\widetilde{\omega}_r\, a^\dagger a + \frac{1}{2!}(E_{J,0}\cos\phi_{\mathrm{dc}})\phi_0^2\left(a^{\dagger 2} + a^2\right)\\ &- \frac{1}{2!}(E_{J,0}\sin\phi_{\mathrm{dc}})\phi_0^2\phi_{\mathrm{ac}}(t)\left(a^\dagger + a\right)^2.\end{aligned} \tag{S19}$$

Note that for the time dependent part we are considering the full Φ^2 potential [cf. Eq. (S12)]. As customary, in order to study the slow dynamics resulting from the modulation, we transform the Hamiltonian into the rotating frame defined by $R(t) = \exp(i\widetilde{\omega}_r a^\dagger a\, t)$, i.e., $H \to H_R = RHR^\dagger + i\dot{R}R^\dagger$:

$$\begin{aligned} H_R(t) \approx & \frac{1}{2!}(E_{J,0}\cos\phi_{\rm dc})\phi_0^2 \left(a^{\dagger 2}\mathrm{e}^{+2i\widetilde{\omega}_r t} + \text{h.c.}\right) \\ & - \frac{1}{2!}(E_{J,0}\sin\phi_{\rm dc})\phi_0^2 \sum_n \left[i\lambda_n \mathrm{e}^{-i(2\widetilde{\omega}_r+\delta_n)t} + \text{h.c.}\right] \\ & \times \left(a^{\dagger 2}\mathrm{e}^{+2i\widetilde{\omega}_r t} + a^2\mathrm{e}^{-2i\widetilde{\omega}_r t} + 2a^\dagger a\right). \end{aligned} \tag{S20}$$

In the rotating wave approximation (RWA) we keep only the slow rotating terms, i.e., those rotating at frequencies much smaller than $\widetilde{\omega}_r$

$$H_{\rm RWA} \approx -\frac{i}{2!}(E_{J,0}\sin\phi_{\rm dc})\phi_0^2 \sum_{n=1}^{2} \lambda_n a^{\dagger 2}\mathrm{e}^{-i\delta_n t} + \text{h.c.} \tag{S21}$$

B. Langevin equation of motion

Introducing the pump frequencies $\omega_{p,i} = 2\widetilde{\omega}_r + \delta_i$, $i = 1, 2$, we can re-write the first-order RWA Hamiltonian (S21) as

$$H_{\rm RWA} = -\frac{i\hbar}{2}\sum_{n=1}^{2}\left[\mu_n^* a^2 \mathrm{e}^{+i(\omega_{p,n}-2\widetilde{\omega}_r)t} - \mu_n a^{\dagger 2}\mathrm{e}^{-i(\omega_{p,n}-2\widetilde{\omega}_r)t}\right], \tag{S22}$$

where we introduce $\mu_n = (E_{J,0}\sin\phi_{\rm dc})\,\phi_0^2\lambda_n/\hbar$ for notational brevity. Now we un-do the rotation transformation $R(t)$ which leads us to

$$H \approx \hbar\widetilde{\omega}_r a^\dagger a - \frac{i\hbar}{2}\sum_{n=1}^{2}\left(\mu_n^* a^2\mathrm{e}^{+i\omega_{p,n}t} - \mu_n a^{\dagger 2}\mathrm{e}^{-i\omega_{p,n}t}\right). \tag{S23}$$

From here we derive the Heisenberg equation of motion $\partial_t\, a = i[H, a]/\hbar$. For convenience, we work in the frequency domain defined by

$$a[\omega] = \int_{-\infty}^{+\infty} \mathrm{d}t\, \mathrm{e}^{i\omega t}\, a(t). \tag{S24}$$

Therefore, the Langevin equation of motion is

$$\left[\frac{\kappa}{2} - i(\omega - \widetilde{\omega}_r)\right] a[\omega] - \sum_{n=1}^{2}\mu_n a^\dagger[\omega_{p,n} - \omega] = -\sqrt{\kappa}a_{\rm in}[\omega], \tag{S25}$$

where we included the presence of the environment with the external decay rate κ of the resonator (ignoring internal losses) and $a_{\rm in}$ the input operator [14]. This equation tells us that for every "signal" frequency ω there are two "idlers" with frequencies $\omega_{p,1} - \omega$ and $\omega_{p,2} - \omega$.

C. Frequency comb output correlations

The idea now is to characterize the output correlations resulting from the mixing of equally spaced input signal frequencies, i.e., a *frequency comb*. This follows from studying the output frequency components given by the input-output equation $a_{\rm out}[\omega] = a_{\rm in}[\omega] + \sqrt{\kappa}a[\omega]$ [14]. In order to do this we need to first define the frequency comb.

We start by introducing the following notation $\delta_1 = -\delta_2 \equiv -\Delta/2$. In terms of Δ the pump frequencies can be re-written as

$$\begin{aligned} \omega_{p,1} &= 2\widetilde{\omega}_r - \Delta/2 \\ \omega_{p,2} &= 2\widetilde{\omega}_r + \Delta/2. \end{aligned}$$

Without loss of generality we assume $\delta > 0$ and therefore $\omega_{p,2} > \omega_{p,1}$.

The frequency comb is defined as an equally spaced set of frequencies labelled by an integer index n

$$\omega_n = \omega_0 + n\,\delta.$$

We choose the center of the comb as $\omega_0 \equiv (\omega_{p,1} + \omega_{p,2})/4 = \widetilde{\omega}_r$ and its spacing δ as

$$\begin{aligned} \delta &\equiv \frac{\omega_{p,2}}{2} - \omega_0 = \omega_0 - \frac{\omega_{p,1}}{2} \\ &= \frac{\omega_{p,2} - \omega_{p,1}}{4} = \frac{\Delta}{4}. \end{aligned} \tag{S26}$$

Following Eq. (S25), for a signal ω in the frequency comb, i.e., $\omega = \omega_n$, the two idlers are located at $\omega_{p,1} - \omega_n$ and $\omega_{p,2} - \omega_n$. We can rewrite these as

$$\begin{aligned} \omega_{p,1} - \omega_n &= 2\omega_0 - 2\delta - (\omega_0 + n\delta) \\ &= \omega_0 - (n+2)\delta \\ &= \omega_{-n-2} \end{aligned}$$

and

$$\begin{aligned} \omega_{p,2} - \omega_n &= 2\omega_0 + 2\delta - (\omega_0 + n\delta) \\ &= \omega_0 - (n-2)\delta \\ &= \omega_{-n+2}, \end{aligned}$$

in other words the idlers are also within the frequency comb with an index spacing of ±2. Therefore, if n is an even (odd) integer, it will only be coupled to other even (odd) frequencies, or equivalently, there will be *no correlations* between even and odd indices in the frequency comb. Furthermore, while the two pumps connect all even modes with each other, the odd ones are split into two subsets:

$$\{\cdots -11, -7, -3, +1, +5, +9, \dots\}$$
$$\{\cdots -9, -5, -1, +3, +7, +11, \dots\}$$

See Fig. **??** in the main text for a visual rendition of the correlation across modes in the comb.

Finally, by introducing the notation $a[\omega_n] \equiv a_n$ for the frequency-domain operators, we rewrite the Langevin equation (S25) for the frequency comb as:

$$\chi_n^{-1} a_n - \mu_1 a^\dagger_{-2-n} - \mu_2 a^\dagger_{-n+2} = -\sqrt{\kappa} a_n^{\mathrm{in}}, \tag{S27}$$

with $\chi_n = [\kappa/2 - i(\omega_n - \widetilde{\omega}_r)]^{-1}$.

In order to solve for $a_{\mathrm{out}}[\omega_n] \equiv a_{\mathrm{out},n}$, we can write the system (S27) in matrix form

$$M\boldsymbol{a} = -\sqrt{\kappa}\boldsymbol{a}_{\mathrm{in}}, \tag{S28}$$

with $\boldsymbol{a}^\top = (\ldots, a_{-1}, a_0, a_{+1}, \ldots, a^\dagger_{-1}, a^\dagger_0, a^\dagger_{+1}, \ldots)$ and similarly for $\boldsymbol{a}_{\mathrm{in}}$ and $\boldsymbol{a}_{\mathrm{out}}$. From the above equation we have $\boldsymbol{a} = -\sqrt{\kappa} M^{-1} \boldsymbol{a}_{\mathrm{in}}$. The solution for the output frequency components follows from the input-output relation

$$\begin{aligned} \boldsymbol{a}_{\mathrm{out}} &= \boldsymbol{a}_{\mathrm{in}} + \sqrt{\kappa}\boldsymbol{a} \\ &= (\mathbb{I} + \kappa M^{-1})\boldsymbol{a}_{\mathrm{in}} = S\boldsymbol{a}_{\mathrm{in}}. \end{aligned} \tag{S29}$$

The quadrature operators $x_n = b_n^\dagger + b_n$ and $p_n = i(b_n^\dagger - b_n)$ can be obtained via the linear transformation $\boldsymbol{r} = K\boldsymbol{b}$ with $\boldsymbol{b} = \boldsymbol{a}$, $\boldsymbol{a}_{\mathrm{in}}$, $\boldsymbol{a}_{\mathrm{out}}$ and the matrix K given by

$$K = \begin{pmatrix} \mathbb{I}_n & \mathbb{I}_n \\ -i\mathbb{I}_n & i\mathbb{I}_n \end{pmatrix}, \tag{S30}$$

when the quadratures are arranged in the (x, p) ordering $\boldsymbol{r} = (x_1, \ldots, x_n, p_1, \ldots, p_n)$.

The linear relation between input and output modes (S29) is a consequence of having neglected the non-linear contributions from the SQUID potential. This linear transformation will convert an input thermal (Gaussian) state into an output Gaussian state as well. A Gaussian state is completely characterized by its first and second order moments, the latter being known as the covariance matrix V. The covariance matrix is defined as

$$V = \frac{1}{2}\langle \boldsymbol{r}\cdot\boldsymbol{r}^\top + (\boldsymbol{r}\cdot\boldsymbol{r}^\top)^\top \rangle, \tag{S31}$$

in terms of the quadrature vector $\boldsymbol{r}$. From Eqs. (S29) and (S30) we can define a linear transformation between input and output quadrature operators

$$\boldsymbol{r}_{\mathrm{out}} = A\boldsymbol{r}_{\mathrm{in}}, \tag{S32}$$

from which we have

$$\boldsymbol{r}_{\mathrm{out}} \cdot \boldsymbol{r}_{\mathrm{out}}^\top = A\boldsymbol{r}_{\mathrm{in}}(A\boldsymbol{r}_{\mathrm{in}})^\top = A(\boldsymbol{r}_{\mathrm{in}} \cdot \boldsymbol{r}_{\mathrm{in}}^\top)A^\top.$$

Therefore, the input and output covariance matrices relate as

$$V_{\mathrm{out}} = AV_{\mathrm{in}}A^\top. \tag{S33}$$

If we assume the input modes to be in the vacuum state, then $V_{\mathrm{in}} = \mathbb{I}$.

The theory matrix in Fig. **??** is given by Eq. (S33), where we assume the input state to be vacuum. Hence, the output covariance matrix V_{out} is determined by matrix A, which is in turn set by the parameters μ_1, μ_2, ω_n, κ and $\tilde{\omega}_r$. Since the parameters $\kappa = 2\pi \cdot 124\,\mathrm{MHz}$ and $\tilde{\omega}_r = 2\pi \cdot 4.3\,\mathrm{GHz}$ are obtained from a frequency spectroscopy sweep, and ω_n is set by the experimentalist, this leaves us with only two parameters, μ_1 and μ_2, which are complex effective couplings between modes and controlled by the two flux pumps. We adjust these values by hand, obtaining good correspondence between experiment and theory with $\mu_1 = 2\pi \cdot 15.6\angle 90^\circ$ MHz and $\mu_2 = 2\pi \cdot 15.6\angle -60^\circ$ MHz.

D. Gaussianity of measured noise

Our theoretical model and experimental analysis considers the noise to be Gaussian. A distribution is Gaussian if it is completely characterized by the first two moments. We therefore check for Gaussianity by also calculating the third and fourth order moments in our data, called the skewness and kurtosis. We use the `scipy.stats`-package [15, 16] to test the distribution of I- and Q-quadratures at each frequency. The result is presented in Fig. S6. Skew and kurtosis are zero for an ideal Gaussian distribution. We see that all values (for all quadratures and all frequencies) are small. But are these values are small enough given the number of data points? To answer this question we do a skew and kurtosis test, where our null hypothesis is that our data is drawn from a Gaussian distribution. The right-hand column in Fig. S6 presents the p-value for this hypothesis test. Since a majority of the p-values are larger than 0.1 we have a high level of confidence that our data is sampled from a Gaussian distribution.

VI. MULTIPARTITE ENTANGLEMENT

A. Bipartite entanglement criteria

In Fig. **??**b we compared three entanglement tests: the Duan criterion, the PPT test and the SvL test. Consider two Gaussian states A and B residing in the joint Hilbert space $\mathcal{H}_A \otimes \mathcal{H}_B$. With our choice of normalization, the Duan criterion is [17]

$$\langle(\Delta u)^2\rangle + \langle(\Delta v)^2\rangle - 4 \geq 0, \tag{S34}$$

where $u = x_A + x_B$ and $v = p_A - p_B$. The quadrature operators $x_{A/B}$ and $p_{A/B}$ satisfy the commutation relations $[x_A, p_A] = [x_B, p_B] = 2i$ and the mean is taken over the bipartite state described by the covariance matrix V_{AB}.

The Duan criteria is a necessary and sufficient condition for separability. Another necessary and sufficient condition for separability is the Positive Partial Transpose (PPT) test [18]

$$V^{\mathrm{PPT}} + i\Omega \geq 0, \tag{S35}$$

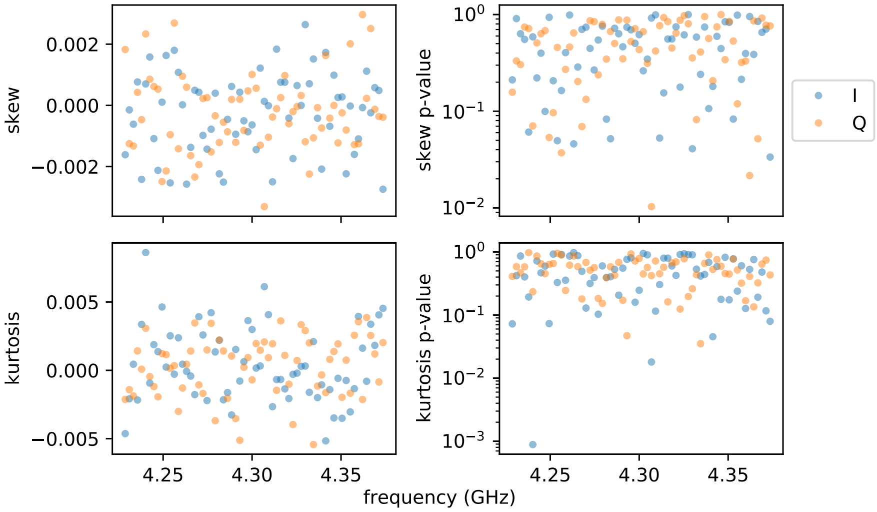

FIG. S6. Skew and kurtosis of our sampled distributions, and the corresponding p-values with our null hypothesis being that our underlying distribution is Gaussian. All skew and kurtosis values are small (ideally zero), and the corresponding p-values mostly greater than 0.1. Hence we deduce that distribution underlying our measured data is indeed Gaussian.

where $V^{\rm PPT} = \Lambda V_{AB} \Lambda$ and $\Lambda = {\rm diag}(1,1,1,-1)$. Both Duan and PPT criteria apply to bipartite systems and they can not be be used to determine multipartite entanglement. For multipartite entanglement we use the SvL criteria, which tests for arbitrary k-partite entanglement.

B. Genuine multipartite entanglement (GME) and full inseparability

An n-partite mixed state ρ is called *fully separable* if it can be written as a convex combination of product states:

$$\rho = \sum_i p_i \left(\rho_1^i \otimes \rho_2^i \otimes \cdots \otimes \rho_n^i\right), \tag{S36}$$

where $p_i \geq 0$ and $\sum_i p_i = 1$. This is a direct generalization of the definition of separability for bipartite states $n = 2$. In contrast to a bipartite state, which is either entangled or separable, there exists several classes of entanglement and separability for multipartite states. One can arrange the n parts (modes) into $k \leq n$ partitions, which are then considered as subsystems. States that are fully separable with respect to this partition (or can be written as a mixture of such states) are called *k-separable*. A state that is not k-separable is called *k-inseparable* [19]. A state that is not separable with respect to any such split is called fully (n-partite) *inseparable* [20].

Let us consider a tripartite state as an example. It is fully separable if it can be decomposed as

$$\rho = \sum_i p_i \left(\rho_1^i \otimes \rho_2^i \otimes \rho_3^i\right). \tag{S37}$$

It is 2-separable or *biseparable* if it can be written as either of the following states, or a mixture thereof:

$$\begin{aligned} \rho &= \sum_i p_i \left(\rho_{12}^i \otimes \rho_3^i\right), \\ \rho &= \sum_i p_i \left(\rho_{13}^i \otimes \rho_2^i\right), \\ \rho &= \sum_i p_i \left(\rho_{23}^i \otimes \rho_1^i\right), \end{aligned} \tag{S38}$$

where ρ_{12}^i, ρ_{13}^i and ρ_{23}^i are bipartite states. They can be either entangled or separable but in the latter case we will actually have the above fully separable case. In general $(k+1)$-separability implies k-separability [21]. Note that if the state is a statistical mixture of all three states (S38), there is no *single* bipartite split with respect to which the state is separable, but the state is nonetheless biseparable since it is a mixture of biseparable states [22].

If a state is not biseparable, it is said to be *genuinely multipartite entangled* (GME). That is because it implies entanglement for any other partitioning of modes. For pure states, GME is equivalent to full inseparability. This is not the case for mixed states. In this context, GME implies full inseparability, but not the other way around. Hence GME is a stronger form of correlation [23].

The SvL test result of Fig. **??** show that none of our bipartitions are separable, which suggests we are generating fully inseparable states [24–26], but not necessarily GME as we have not ruled out mixtures of biseparable states.

C. GME in lossy systems

It is known that testing for GME is more sensitive to imperfections of the experiment, in comparison with other measurements of entanglement [27, 28]. To explore this effect we simulate losses by mixing a signal with an auxiliary mode in the vacuum or a thermal state at a fictitious beam-splitter. After the beam-splitter, the reflected mode is lost and we are left with the transmitted one. The beam-splitter transmissivity η determines what fraction of the original signal is transmitted with $\eta = 1$ corresponding to the lossless case while $\eta < 1$ implies the presence of losses, which in an experimental setting could stem from cryogenic electronics such as cables and isolators. We combine n modes from an ideal covariance matrix V_{ideal} (calculated according to the theory in Sec. V C) with vacuum $\mathbb{I}_{2n}$. The covariance matrix of the beam-splitter input is the direct sum of $V_{\mathbf{ideal}}$ and I_{2n}

$$V = \begin{pmatrix} V_{\mathbf{ideal}} & 0 \\ 0 & \mathbb{I}_{2n} \end{pmatrix}. \tag{S39}$$

The state transforms as

$$V' = SVS^{\top} \tag{S40}$$

under the beam-splitter transformation S, which is given by [29]

$$\begin{pmatrix} \cos\theta \mathbb{I}_{2n} & \sin\theta \mathbb{I}_{2n} \\ -\sin\theta \mathbb{I}_{2n} & \cos\theta \mathbb{I}_{2n} \end{pmatrix}, \tag{S41}$$

with $\eta = \cos^2\theta$. After the vacuum modes are mixed in and traced out, we select a subset of 5 modes and calculate the purity $p(V) = 1/\sqrt{|V|}$ [29] as well as the entanglement witness. Here we use the program `FullyWit` that tests for full separability, and `MultiWit` that tests for GME, both from Ref. [30]. The results shown in Fig. S7 for different levels of vacuum noise.

Selecting only a subset of modes from a larger entangled system causes a reduction of purity. In this example with five modes, the initial purity is $p = 0.5410$. In Fig. S7, we show how the witnesses of full separability and GME change as η is reduced, meaning more vacuum is mixed into the state. When the full separability witness is negative, it means the state is not fully separable, i.e. there is some type of entanglement in the state. If the GME witness is negative it means the state is genuinely multipartite entangled. It can be seen that the full separability witness increases linearly with the reduced η, but remains negative until $\eta = 0$ when the state is fully vacuum. However, the state is genuinely multipartite entangled only until $\eta = 0.64$ corresponding to a purity of 0.31.

Our example shows that it is in theory possible to generate GME states using our method, provided that the purity is not too low. An analysis of our data however, reveals that the K^{-1} sets have an average purity of 0.20, while for K^1 and K^0 it is 0.16 and 0.06 respectively. It is therefore unlikely our current dataset exhibits GME. An application of the Hyllus and Eisert test [30] to our data provides no strong evidence for GME. Future research should improve on the experimental methodology to enable states with higher purity.

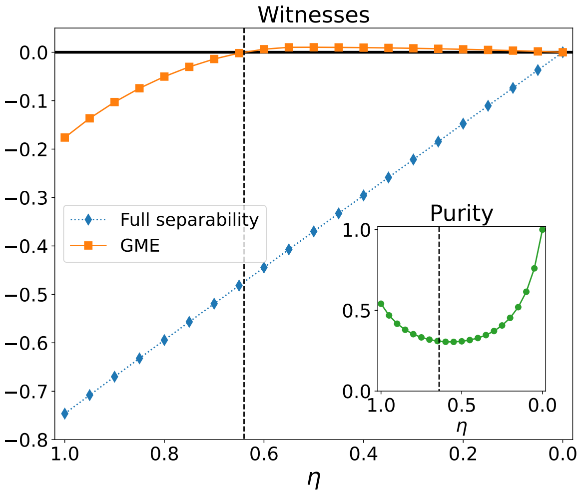

FIG. S7. Witnesses of full separability and GME for increasing amounts of vacuum mixed into an ideal state of five even modes, as a function of beam splitter transmittivity η. The state is never fully separable except for $\eta = 0$ when the state is completely vacuum, but GME is only present until the purity has decreased to 0.31, indicated by the vertical dashed line. The inset shows purity which decreases as more vacuum is mixed into the state, and then increases after $\eta = 0.5$ as the state becomes more and more dominated by vacuum.

---

[1] "Intermodulation products." `https://intermodulation-products.com/`. Accessed: 2021-10-19.

[2] E. A. Tholén, D. Platz, D. Forchheimer, V. Schuler, M. O. Tholén, C. Hutter, and D. B. Haviland, "Note: The intermodulation lockin analyzer," *Review of Scientific Instruments*, vol. 82, no. 2, p. 026109, 2011.

[3] "Multifrequency lockin basics." `https://www.intermod.pro/manuals/IMP-MLA_user_manual/lockin.html`. Accessed: 2022-11-13.

[4] S. W. Jolin, R. Borgani, M. O. Tholén, D. Forchheimer, and D. B. Haviland, "Calibration of mixer amplitude and phase imbalance in superconducting circuits," *Review of Scientific Instruments*, vol. 91, no. 12, p. 124707, 2020.

[5] M. Mariantoni, E. P. Menzel, F. Deppe, M. A. Araque Caballero, A. Baust, T. Niemczyk, E. Hoffmann, E. Solano, A. Marx, and R. Gross, "Planck spectroscopy and quantum noise of microwave beam splitters," *Phys. Rev. Lett.*, vol. 105, p. 133601, Sep 2010.

[6] E. Tholén, *Intermodulation in microresonators for microwave amplification and nanoscale surface analysis.* PhD thesis, KTH, Sweden, 2009.

[7] A. A. Clerk, M. H. Devoret, S. M. Girvin, F. Marquardt, and R. J. Schoelkopf, "Introduction to quantum noise, measurement, and amplification," *Rev. Mod. Phys.*, vol. 82, pp. 1155–1208, Apr 2010.

[8] C. M. Caves, "Quantum limits on noise in linear amplifiers," *Phys. Rev. D*, vol. 26, pp. 1817–1839, Oct 1982.

[9] F. Lecocq, L. Ranzani, G. A. Peterson, K. Cicak, R. W. Simmonds, J. D. Teufel, and J. Aumentado, "Nonreciprocal microwave signal processing with a field-programmable josephson amplifier," *Phys. Rev. Applied*, vol. 7, p. 024028, Feb 2017.

[10] A. Pastore, "An introduction to bootstrap for nuclear physics," *Journal of Physics G: Nuclear and Particle Physics*, vol. 46, p. 052001, Apr 2019.

[11] A. Agrawal, R. Verschueren, S. Diamond, and S. Boyd, "A rewriting system for convex optimization problems," *Journal of Control and Decision*, vol. 5, no. 1, pp. 42–60, 2018.

[12] S. Diamond and S. Boyd, "CVXPY: A Python-embedded modeling language for convex optimization," *Journal of Machine Learning Research*, vol. 17, no. 83, pp. 1–5, 2016.

[13] "`scipy.optimize.differential_evolution`." `https://docs.scipy.org/doc/scipy/reference/generated/scipy.optimize.differential_evolution.html`. Accessed: 2022-09-11.

[14] C. W. Gardiner and M. J. Collett, "Input and output in damped quantum systems: Quantum stochastic differential equations and the master equation," *Phys. Rev. A*, vol. 31, pp. 3761–3774, Jun 1985.

[15] "`scipy.stats.skewtest`." `https://docs.scipy.org/doc/scipy/reference/generated/scipy.stats.skewtest.html`. Accessed: 2022-07-19.

[16] "`scipy.stats.kurtosistest`." `https://docs.scipy.org/doc/scipy/reference/generated/scipy.stats.kurtosistest.html`. Accessed: 2022-07-19.

[17] L.-M. Duan, G. Giedke, J. I. Cirac, and P. Zoller, "Inseparability criterion for continuous variable systems," *Phys. Rev. Lett.*, vol. 84, pp. 2722–2725, Mar 2000.

[18] R. Simon, "Peres-horodecki separability criterion for continuous variable systems," *Phys. Rev. Lett.*, vol. 84, pp. 2726–2729, Mar 2000.

[19] M. Seevinck and J. Uffink, "Partial separability and entanglement criteria for multiqubit quantum states," *Phys. Rev. A*, vol. 78, p. 032101, Sep 2008.

[20] W. Dür and J. I. Cirac, "Classification of multiqubit mixed states: Separability and distillability properties," *Phys. Rev. A*, vol. 61, p. 042314, Mar 2000.

[21] Y. Hong and S. Luo, "Detecting k-nonseparability via local uncertainty relations," *Phys. Rev. A*, vol. 93, p. 042310, Apr 2016.

[22] M. Huber, F. Mintert, A. Gabriel, and B. C. Hiesmayr, "Detection of High-Dimensional Genuine Multipartite Entanglement of Mixed States," *Phys. Rev. Lett.*, vol. 104, p. 210501, May 2010.

[23] R. Y. Teh and M. D. Reid, "Criteria to detect genuine multipartite entanglement using spin measurements," *Phys. Rev. A*, vol. 100, p. 022126, Aug 2019.

[24] S. Gerke, J. Sperling, W. Vogel, Y. Cai, J. Roslund, N. Treps, and C. Fabre, "Multipartite Entanglement of a Two-Separable State," *Phys. Rev. Lett.*, vol. 117, p. 110502, Sep 2016.

[25] L. K. Shalm, D. R. Hamel, Z. Yan, C. Simon, K. J. Resch, and T. Jennewein, "Three-photon energy–time entanglement - Nature Physics," *Nat. Phys.*, vol. 9, pp. 19–22, Jan 2013.

[26] R. Y. Teh and M. D. Reid, "Criteria for genuine N-partite continuous-variable entanglement and Einstein-Podolsky-Rosen steering," *Phys. Rev. A*, vol. 90, p. 062337, Dec 2014.

[27] O. Gühne and G. Tóth, "Entanglement detection," *Phys. Rep.*, vol. 474, pp. 1–75, Apr 2009.

[28] T. Aoki, N. Takei, H. Yonezawa, K. Wakui, T. Hiraoka, A. Furusawa, and P. van Loock, "Experimental Creation of a Fully Inseparable Tripartite Continuous-Variable State," *Phys. Rev. Lett.*, vol. 91, p. 080404, Aug 2003.

[29] A. Serafini, *Quantum Continuous Variables: A Primer of Theoretical Methods.* Andover, England, UK: Taylor & Francis, Oct 2017.

[30] P. Hyllus and J. Eisert, "Optimal entanglement witnesses for continuous-variable systems," *New J. Phys.*, vol. 8, p. 51, Apr 2006.